ACS APPLIED MATERIALS & INTERFACES

Research Article

www.acsami.org

Optical Engineering of Uniformly Decorated Graphene Oxide Nanoflakes via in Situ Growth of Silver Nanoparticles with Enhanced Plasmonic Resonance

Kai Yuan,[†] Lie Chen,[†,‡] and Yiwang Chen*[,†,‡]

[†]College of Chemistry/Institute of Polymers and [‡]Jiangxi Provincial Key Laboratory of New Energy Chemistry, Nanchang University, 999 Xuefu Avenue, Nanchang 330031, China

Supporting Information

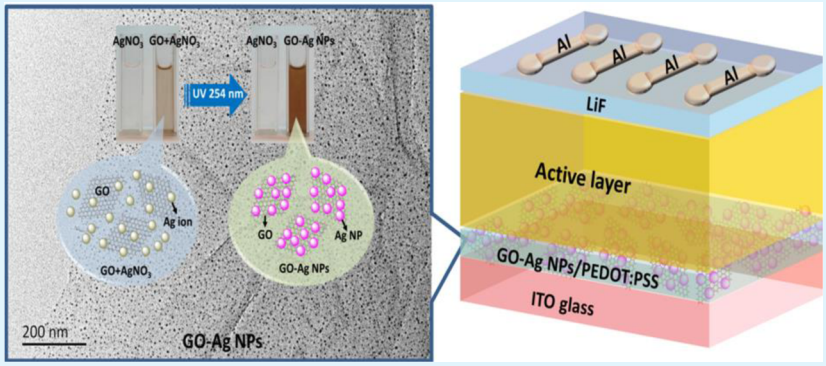

ABSTRACT: A nanocomposite of silver-nanoparticle-decorated graphene oxide (GO−Ag NPs), enhanced by the surface plasmon resonance (SPR) effect, improved the performance of polymer solar cells (PSCs). The GO−Ag NPs were fabricated in situ via ultraviolet (UV) irradiation (254 nm) of GO and an aqueous solution of $AgNO_3$. The photoexcited GO accelerated reduction of Ag^+ ions into silver nanoparticles (Ag NPs) upon UV irradiation, and the Ag NPs spontaneously deposited on the GO nanoflakes because the numerous functional groups on GO enable efficient adsorption of Ag^+ ions and Ag NPs via electrostatic interactions. The strong coupling between the SPR effect of GO−Ag NPs and incident light offers the probability of improved light absorption and corresponding exciton generation rate with enhanced charge collection, resulting in significant enhancement in short-circuit current density and power conversion efficiency (PCE). Therefore, the PCE of PSCs based on poly[4,8-bis(2-ethylhexylthiophene-5-yl)-benzo[1,2-*b*:4,5-*b*]dithiophene-2,6-diyl]-*alt*-[2-(2-ethylhexanoyl)thieno[3,4-*b*]-thiophen-4,6-diyl] and [6,6]-phenyl C_{71}-butyric acid methyl ester has been substantially elevated to 7.54% from 6.58% by introducing GO−Ag NPs at the indium tin oxide/poly(3,4-ethylenedioxythiophene):polystyrene sulfonic acid interface. In addition, the excellent properties of GO−Ag NPs, including its simple preparation, processability in aqueous solution, cost-effectiveness, and sustainability, make it suitable for the roll-to-roll manufacturing of PSCs.

KEYWORDS: *graphene oxide, surface plasmon resonance, polymer solar cells, light absorption, exciton generation rate*

INTRODUCTION

Polymer solar cells (PSCs) based on bicontinuous networks of a bulk heterojunction (BHJ) blend of a semiconducting conjugated polymer donor and a fullerene derivative acceptor are promising candidates for solar energy conversion and have drawn considerable attention, owing to their attractive properties, including their potential to be inexpensive and sustainable, lightweight and highly flexible, low-temperature solution processable, and printable for large-scale fabrication by roll-to-roll techniques.[1−5] In recent years, the power conversion efficiency (PCE) of PSCs has been dramatically improved and has already reached over 9% for single stack devices and beyond 10% for tandem structures by designing new semiconducting light-absorbing conjugated polymer donor materials, controlling the photoactive layers' morphology, and optimizing and tailoring device architectures and interface engineering for devices.[6−18] Despite the rapid development of PSCs and significant improvement in PCE, further improvement of photovoltaic performance is still required for commercialization.

The overall PCE of PSCs is governed by the light-trapping efficiency and internal quantum efficiency (IQE) of the devices.[19,20] The IQE of state-of-art devices can approach 100% by modifying diffusion and dissociation of excitons generated in the active layer and charge collection at corresponding electrode contacts.[21] Thus, the light-trapping

Received: September 2, 2014
Accepted: November 12, 2014
Published: November 12, 2014

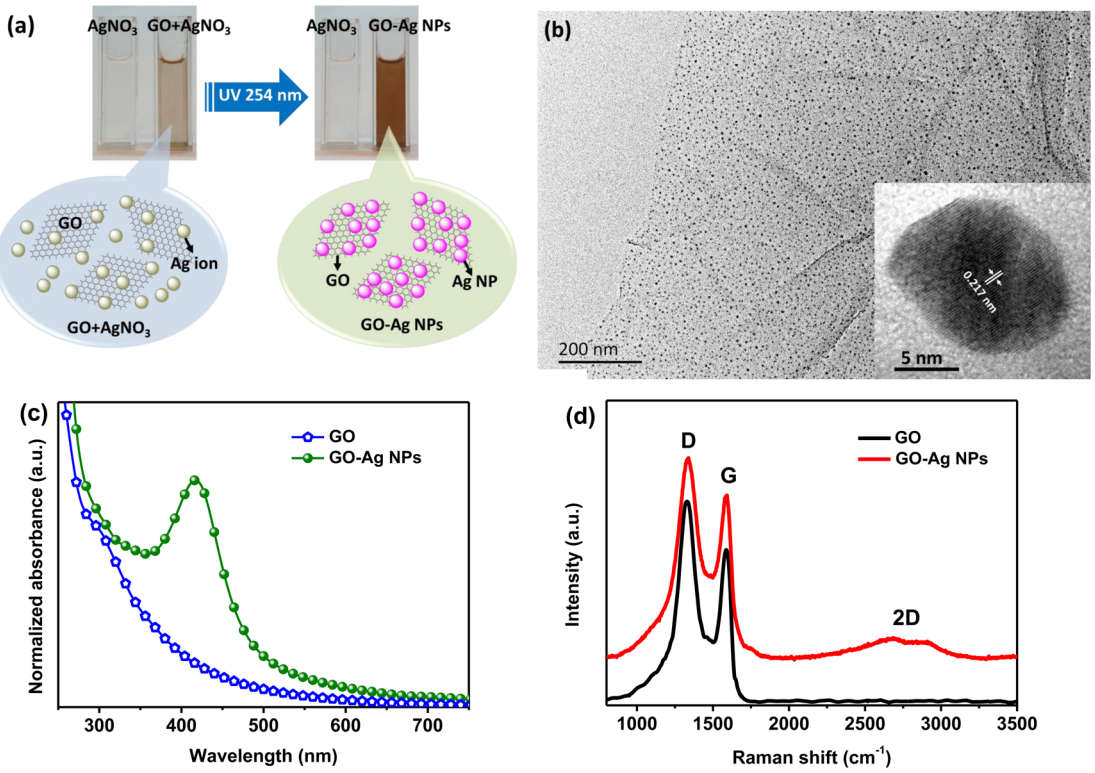

Figure 1. (a) Photographs and schematic illustration of $AgNO_3$ and GO + $AgNO_3$ solutions before (left) and after (right) ultraviolet irradiation. (b) TEM and HR-TEM (inset of b) images of GO−Ag nanoparticles prepared by 25 min of UV irradiation. The distinguishable lattice fringe of silver nanoparticles is at 0.217 nm, as show in the HR-TEM image. (c) Comparison of UV−vis absorption spectra of GO and GO−Ag NPs aqueous solution. (d) Raman spectra of GO and GO−Ag NPs.

efficiency of the incident light continues to be one of the primary obstacles of current PSC devices toward realizing high PCE. Generally, the optimal thickness for the photoactive layer of a PSC device is approximately 100 nm for effective charge collection and minimizing the charge-recombination loss. However, such a thin photoactive layer can result in failure to complete harvesting of the incoming solar irradiation.[6] Therefore, employing a thicker photoactive layer is an alternative approach for improving light absorption efficiency. Unfortunately, due to the relatively low mobilities and short exciton diffusion lengths of semiconducting organic materials, the charge-recombination loss and rapid decrease in IQE inevitably increase.[21] Consequently, the trade-off between charge extraction and light-trapping efficiencies becomes one of the major bottlenecks.

In order to overcome this problem, lots of approaches for increasing light-trapping without influencing the charge extraction efficiency have been developed.[16] For instance, employing folded device architectures to prolong the optical length, using optical spacers to spatially redistribute the optical electrical field in the device, and incorporating the surface plasmon resonance (SPR) effect caused by plasmonic nanostructures have been successful.[21,22] Among these available tactics for improving light-trapping, the SPR effect of plasmonic nanostructures, which can effectively stockpile incident light energy via localized surface plasmon modes and improve the photogeneration of excitons, has attracted much attention.[22−25] The plasmonic nanostructures can be incorporated into the active layer, the hole transport layer (HTL), and at the interface of anode/HTL or HTL/active layer.[19,23−25] Generally, to take full advantage of the SPR effect to improve device performance, the plasmonic nanostructures are usually embedded at the anode/HTL interface owing to the exciton quenching occurring via nonradiative energy transfer when the distance between plasmonic nanostructures and active layer is too close.[23] Therefore, the plasmonic nanostructures have been frequently embedded in the buffer layer [such as poly(3,4-ethylenedioxythiophene):polystyrene sulfonic acid (PEDOT:PSS)] or introduced to the interface between the buffer layer and the indium tin oxide (ITO).

Graphene oxide (GO), a two-dimensional structure possessing many unique properties, including high strength and durable, low cost, solution processability, various oxygen-containing functional groups (e.g., hydroxyl, carbonyl, carboxyl, and epoxide units), and easy functionalization, has been considered to be a promising interfacial material for highly efficient PSCs.[26−30] Recently, stable and high-performance PSCs have been successfully fabricated with stretchable GO and GO-based composites as electron- and/or hole-extraction layers.[26−28] Li et al. first reported using solution-processable GO instead of PEDOT:PSS as efficient HTL to improve the performance of PSCs, and they discovered that the leakage current can be effectively suppressed by GO and the hole and electron recombination rate lowered.[31] Yun et al. employed reduced GO (rGO) as the hole-extraction layer to fabricate PSCs that have preferable stability compared to the corresponding ones using PEDOT:PSS.[32] Liu et al. developed the GO derivative cesium-neutralized graphene oxide (GO−Cs), which served as both HTL and ETL for high-performance PSCs.[28] Recently, nanocomposites based on GO (or rGO) and metal nanoparticles (such as Ag−GO, Ag−rGO, and Au−GO) have drawn wide attention due to their extensive applications

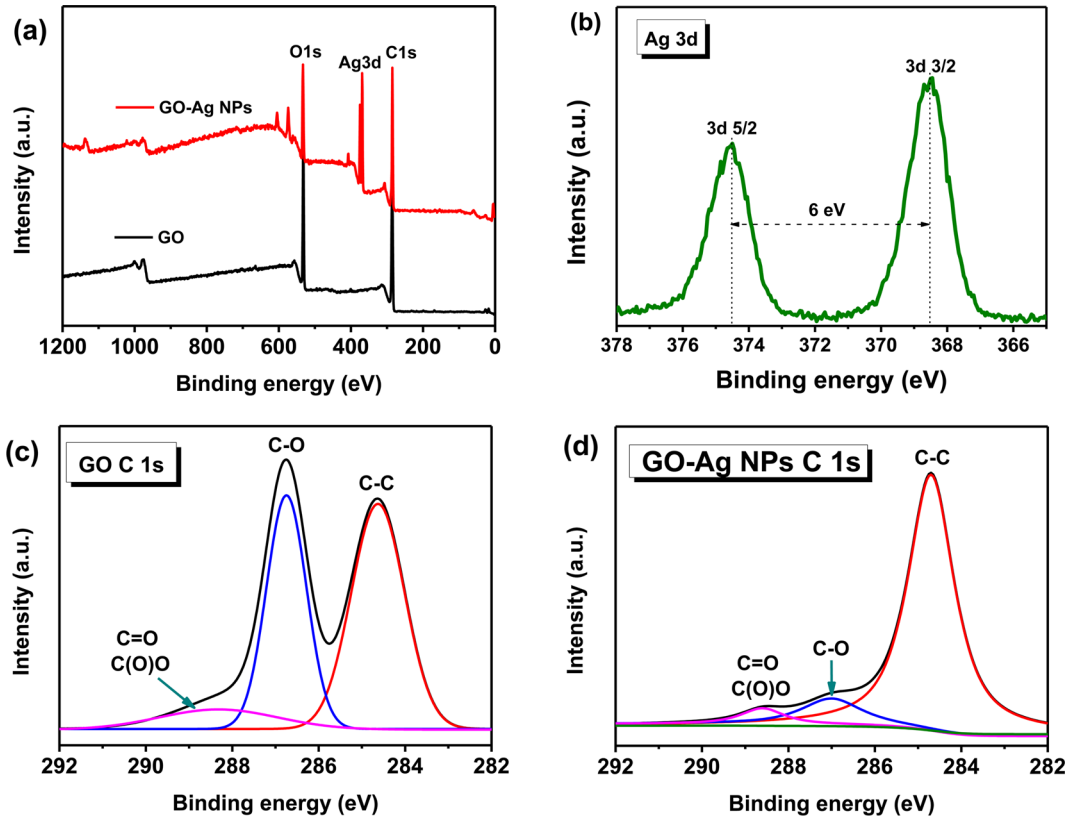

Figure 2. (a) XPS spectra of GO and GO−Ag NPs and (b) the Ag 3d region of GO−Ag NPs film. XPS spectra of the C 1s region obtained from (c) GO and (d) GO−Ag NPs.

in, for example, photodetectors, sensors, biomaterials, photocatalysts, and photovoltaic devices.[33−37]

Herein, we make an attempt to elevate the performance of PSCs through incorporating silver-nanoparticle-decorated graphene oxide (GO−Ag NPs) with SPR enhancement. The GO−Ag NPs featured several excellent properties. First, the GO−Ag NPs can be in situ synthesized in one-step by ultraviolet (UV) irradiation of GO and an aqueous $AgNO_3$ solution. During UV irradiation, the photoexcited GO can accelerate reduction of Ag^+ ions into silver nanoparticles (Ag NPs), and the high surface area of GO with numerous functional groups enables efficient adsorption of Ag^+ ions via electrostatic interactions, and at the same time, GO also acts as a template for the anchor of Ag NPs to afford silver-nanoparticle-decorated GO. Second, the GO−Ag NPs are promising for large-scale, roll-to-roll manufacturing of printable PSCs due to their solution processability. In addition, the strong coupling between the SPR effect of GO−Ag NPs and the incident light offers the increased probability of light absorption and the corresponding improvement of exciton generation rate, leading to significant enhancement in short-circuit current density and PCE. Therefore, the PCE of PSCs based on poly[4,8-bis(2-ethylhexylthiophene-5-yl)benzo[1,2-*b*:4,5-*b*]dithiophene-2,6-diyl]-*alt*-[2-(2-ethylhexanoyl)thieno-[3,4-*b*]thiophen-4,6-diyl] (PBDTTT-C-T)[38] and [6,6]-phenyl C_{71}-butyric acid methyl ester ($PC_{71}BM$) has been substantially elevated to 7.54% from 6.58% by introducing GO−Ag NPs at the ITO/PEDOT:PSS interface.

RESULTS AND DISCUSSION

Among various available approaches, ultraviolet (UV) irradiation of the mixture of GO and $AgNO_3$ solution was selected to synthesize the GO−Ag NPs nanocomposites.[39−45] The GO nanoflakes were photoexcited with UV irradiation in the presence of $AgNO_3$ solution, in which the Ag^+ ions were reduced to Ag NPs through electron transfer from the photoexcited GO. During this process, the Ag NPs tend to form and grow in situ on the GO nanoflakes' surfaces (Figure 1a). After UV irradiation, the GO and $AgNO_3$ mixture turned dark brown, suggesting the transformation of Ag^+ ions to Ag NPs [Figures 1a and S1 (Supporting Information)]. Details of the synthesis of GO−Ag NPs nanocomposites are provided in the Experimental Section. The transmission electron microscopy (TEM) and high-resolution transmission electron microscopy (HR-TEM) images of the GO−Ag NPs are presented in Figure 1b. The Ag NPs have an average diameter of ca. 11 nm with distinguished lattice fringes of 0.217 nm, corresponding to the (111) lattice plane of Ag. The TEM images [Figures 1b and S2 (Supporting Information)] confirmed that the GO−Ag NPs possessed the property of flexible two-dimensional sheets, and at the same time, the Ag NPs with uniform sizes homogeneously decorated the surface of the GO nanoflakes without agglomeration, and no free Ag NPs are formed outside the GO nanoflakes. The comparison of the UV−vis absorption spectra of GO and GO−Ag NPs aqueous solutions are presented in Figure 1c. After UV irradiation, the specific surface plasmon resonance (SPR) peak of the Ag NPs at about 420 nm was observed in the GO−Ag NPs sample.[46] The comparative TEM and atomic force microscopy (AFM) images of GO and GO−Ag NPs (Figures

dx.doi.org/10.1021/am505916q | ACS Appl. Mater. Interfaces 2014, 6, 21069−21077

S2 and S3, Supporting Information) also support the formation of Ag NPs. Raman spectroscopy measurements were employed to provide additional information on the structural characteristics of the GO−Ag NPs (Figure 1d). The enhanced Raman signals of the GO−Ag NPs compared with the GO is owing to the surface-enhanced Raman scattering effect of the formation of Ag NPs.[47] The defect-induced D bands in the Raman spectra of both GO and GO−Ag NPs are similar, confirming that the formation and decoration of Ag NPs on the GO surface do not significantly introduce any defects into the GO nanoflakes.[47,48]

High-resolution X-ray photoelectron spectroscopy (XPS) was carried out to further provide evidence of the successful formation of GO−Ag NPs as well as the variations of functional groups of the GO nanoflakes' surface (Figure 2). The XPS spectra of C 1s exposit the characteristic features of sp^2 and sp^3 C (284.7 eV), C−O (286.7 eV), and C═O (288.6 eV) groups.[49] In addition, Ag 3d peaks observed at 368.5 and 374.5 eV were determined to be the binding energies of Ag $3d_{5/2}$ and Ag $3d_{3/2}$, respectively. The spin energy separation between the Ag $3d_{5/2}$ and Ag $3d_{3/2}$ electronic states is 6.0 eV (Figure 2b), characteristic of metallic silver, which further confirms the successful formation of Ag NPs upon UV irradiation.[44] According to the deconvoluted C 1s XPS spectra, the integrated area of C−OH groups in the GO−Ag NPs is considerably diminished compared to that in GO upon the UV irradiation and the formation of the Ag NPs, indicating that the hydroxyl groups play an important role in the transformation of Ag^+ ions into Ag NPs.[25] The reduced C−OH groups also confirmed that the GO nanoflakes could be changed to rGO during the UV irradiation and the formation of the Ag NPs.[50,51] Consider that the GO−Ag NPs were thermal annealed at 150 °C for 15 min during the device fabrication. To examine the reduction of GO induced by thermal annealing, we measured the XPS of GO sample after annealing at 150 °C for 15 min (Figure S4, Supporting Information). Due to the thermal instability of GO, we found that the GO indeed was reduced after thermal annealing. By comparing the XPS spectra of GO−Ag NPs with that of GO sample after annealing at 150 °C for 15 min, the thermal reduction of GO was found to be less complete than the photochemical reduction. These results indicated that the reduction of GO was mainly caused by the photochemical reduction process.

Furthermore, to clarify the SPR effect of GO−Ag NPs, steady-state photoluminescence (PL), time-resolved photoluminescence (TRPL), and laser scanning confocal microscopy (LSCM) measurements were performed. Figure 3a shows the steady-state PL spectra for GO and GO−Ag NPs coated on quartz glass substrates. The PL intensity of the GO−Ag NPs was apparently higher than that of GO. The increased PL is probably attributed to the coupling between the plasmonic field induced by the Ag NPs and the excited state of GO nanoflakes. The inset of Figure 3a presents the LSCM image of GO−Ag NPs. The GO−Ag NPs exhibited a bright fluorescence emission under the direct excitation of the laser field. The PL decay profiles performed by TRPL for GO and GO−Ag NPs are presented in Figure 3b. From the decay values, the calculated PL decay time (exciton lifetime) is 369 ps for GO and 478 ps for GO−Ag NPs. The increased exciton lifetime of GO−Ag NPs is consistent with the enhanced steady-state PL intensity, as shown in Figure 3a.

To investigate the function of plasmonic materials of GO−Ag NPs in PSCs, a PBDTTT-C-T:$PC_{71}BM$ blend was employed as the photoactive layer with a device configuration

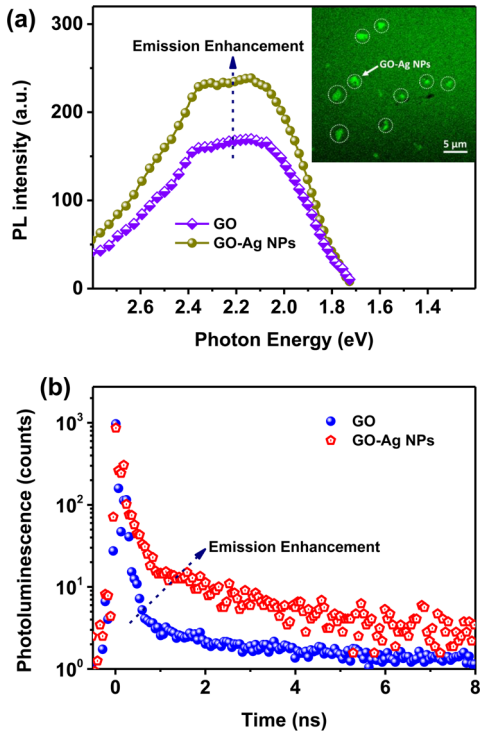

Figure 3. (a) Steady-state photoluminescence spectra and (b) photoluminescence decay profile of GO and GO−Ag nanoparticles. Inset of part a: Laser confocal scanning microscope image of the GO−Ag NPs film.

of ITO/GO−Ag NPs/PEDOT:PSS/PBDTTT-C-T:$PC_{71}BM$/LiF/Al (Figure 4a). A control device with a structure of ITO/PEDOT:PSS/PBDTTT-C-T:$PC_{71}BM$/LiF/Al was also employed for comparison. There are negligible variations in the nanomorphology of the PEDOT:PSS and PBDTTT-C-T:$PC_{71}BM$ layers with the incorporation of GO−Ag NPs (Figure S5, Supporting Information). Figure 4b presents the comparison of the current density−voltage (J−V) characteristics of the devices with and without GO−Ag NPs, and the corresponding detailed photovoltaic parameters of the devices are summarized in Table 1. The device based on PEDOT:PSS, with a short circuit current (J_{sc}) of 14.97 mA cm^{-2}, an open circuit voltage (V_{oc}) of 0.758 V, and a fill factor (FF) of 58.0%, yields a power conversion efficiency (PCE) of 6.58%. Interestingly, the device with GO−Ag NPs exhibits a better photovoltaic performance, showing a J_{sc} of 17.22 mA cm^{-2}, V_{oc} of 0.758 V, and FF of 57.8% and giving a PCE of 7.54%. The inset of Figure 4b presented the inappreciable effect of GO−Ag NPs on the dark J−V characteristics, which indicates the SPR effect of GO−Ag NPs is dominant in the improvement of device performance.[25] This is also supported by the constant work functions before and after incorporation of GO−Ag NPs into the PEDOT:PSS, as determined by ultraviolet photoemission spectroscopy (UPS) measurements (Figure S6, Supporting Information).[24]

To understand which is the key factor (the GO itself or the dispersed Ag NPs) for the enhancement of the solar cells, devices with PEDOT:PSS, GO/PEDOT:PSS, Ag NPs/PEDOT:PSS, and GO−Ag NPs/PEDOT:PSS were fabricated, and the J−V characteristics are summarized in Figure S7 and Table S1 (Supporting Information). From the J−V curves we can see that the performances of the devices were decreased on the basis of GO/PEDOT:PSS devices (PCE = 5.90%)

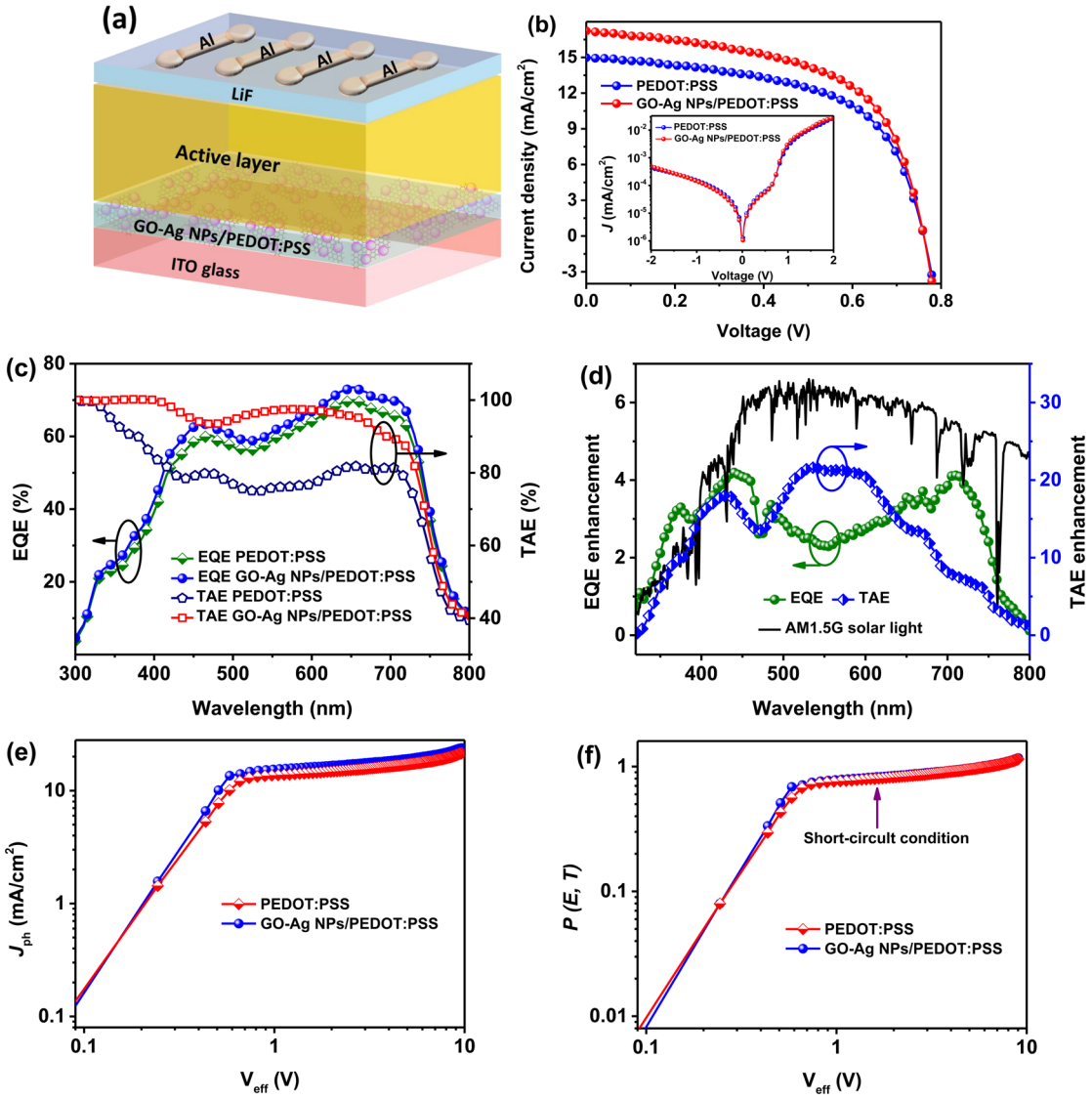

Figure 4. (a) Schematic of the solar cell device. (b) $J-V$ characteristics of PEDOT:PSS- and GO−Ag NPs/PEDOT:PSS-based devices under AM1.5 illumination (at 100 mW/cm^2) and in the dark (inset of part b). (c) EQEs and TAEs of PEDOT:PSS- and GO−Ag NPs/PEDOT:PS- based devices. (d) EQE and TAE enhancements of GO−Ag NPs/PEDOT:PSS-based device over PEDOT:PSS-based device, as well as the photon density of AM1.5G solar light. (e) Photocurrent density (J_{ph}) versus effective voltage (V_{eff}) characteristics of PEDOT:PSS- and GO−Ag NPs/PEDOT:PSS-based devices. (f) Exciton dissociation probability $[P(E,T)]$ as a function of V_{eff} for PEDOT:PSS- and GO−Ag NPs/PEDOT:PSS-based devices.

Table 1. Photovoltaic Properties of the Devices with and without GO−Ag NPs under AM 1.5G Illumination (100 mW cm^{-2})

device	J_{sc}(mA/cm^2)	V_{oc} (V)	*FF* (%)	PCE (%)	$R_s{}^a$ (Ω cm^2)	$R_{sh}{}^a$ (Ω cm^2)
PBDTTT-C-T:PC$_{71}$BM without GO−Ag	14.97	0.758	58.0	6.58	1.9	510.9
PBDTTT-C-T:PC$_{71}$BM with GO−Ag NPs	17.22	0.758	57.8	7.54	2.1	648.7
P3HT:PC$_{61}$BM without GO−Ag	9.26	0.606	65.0	3.65	1.2	937.1
P3HT:PC$_{61}$BM with GO−Ag NPs	10.33	0.606	64.6	4.04	2.3	1452.6

^{a}Series resistance (R_s) and shunt resistance (R_{sh}) were deduced from the $J-V$ curves.

compared to the PEDOT:PSS ones, which is consistent with previously reported results.[37] The devices with Ag NPs/PEDOT:PSS showed a higher PCE (7.11%) than the devices with PEDOT:PSS (6.58%), and the devices with GO−Ag NPs/PEDOT:PSS showed the highest PCE (7.54%). These results indicated that the strong anchoring effect of Ag NPs on the GO surface and the synergistic effect of GO and Ag NPs on the GO−Ag NPs nanostructure are the key factors for enhancement effect.

In order to verify whether GO−Ag NPs or rGO−Ag NPs has a better effect on the performance of the devices, devices based on GO−Ag NPs and rGO−Ag NPs were fabricated and compared. The performance of the devices based on GO−Ag NPs and rGO−Ag NPs were without evident difference, and the corresponding PCE were 7.54% and 7.47%, respectively, as presented in Figure S7 and Table S1 (Supporting Information). During the photochemical reduction process of GO and $AgNO_3$ mixture solution, the GO was partially reduced with the

reduction of the Ag^+ ions, which was confirmed by the XPS spectra of GO and GO−Ag NPs presented in Figure 2. Thus, the structure of GO−Ag NPs and GO−Ag NPs fabricated by photochemical reduction would be without obvious discrepancy. Therefore, there is an inconspicuous difference in the performance of Ag−GO NPs and rGO−Ag NPs based solar cells.

To investigate the effect of the diameter of the Ag NPs on device performance, solar cells based on GO−Ag NPs samples with different UV irradiation times were fabricated. TEM images of different GO−Ag NP samples prepared as a function of UV irradiation time are shown in Figure S8 (Supporting Information). From the TEM data we can see that the diameter and the density of the Ag NPs on the GO surface were increased with increasing UV irradiation time. However, the diameter and the density of the Ag NPs on the GO surface with the UV irradiation time of 60 min (Figure S8, Supporting Information) was almost the same as the sample with the UV irradiation time of 25 min (Figure 1). The reason for the unchanged diameter and density of the Ag NPs on the GO surface was that the very rapidl photochemical reduction process completely finished (all the Ag^+ ions were converted to Ag nanoparticles) after 25 min of UV irradiation, as illustrated by the flowchart of GO−Ag NPs synthesis as a function of UV irradiation time (Figure S1, Supporting Information). The corresponding $J-V$ characteristics are summarized in Figure S9 and Table S2 (Supporting Information). Compared to the devices with GO−Ag NPs after 5 min (PCE = 6.65%) and 10 min (PCE = 6.85%) of UV irradiation, the device with GO−Ag NPs after 25 min of UV irradiation showed the best performance (PCE = 7.54%). In addition, the device with GO−Ag NPs after 60 min of UV irradiation almost had the same performance (PCE = 7.53%) as the device with GO−Ag NPs after 25 min of UV irradiation. Therefore, the diameter of ca. 11 nm was the best choice for the enhanced plasmonic resonance in our case.

The comparison of the photovoltaic parameters indicated that the improvement of PCE is mainly attributed to the enhancement of J_{sc}. To elucidate the origin of the enhancement in J_{sc}, we investigated the spectral responses of the devices. Figure 4c presents the total absorption efficiency (TAE) and external quantum efficiency (EQE) of PEDOT:PSS- and GO−Ag NPs/PEDOT:PSS-based devices. The TAE is calculated from the reflection (R) of the devices using TAE = $1 - R$,[52] and the corresponding device structures for reflectance measurements and the comparison of the reflectance spectra are shown in Figure S10 (Supporting Information). Both the EQE and TAE show an enhancement in a wide range from 350 to 750 nm after incorporating GO−Ag NPs, as presented in the EQE and TAE enhancement (Figure 4d). The result indicated that the increase in J_{sc} can be ascribed to the more efficient exciton generation of the device assisted by the SPR effect of GO−Ag NPs and the contribution of the improved EQE and light harvesting. Furthermore, this result also revealed that the SPR effect of the GO−Ag NPs can regulate the optical properties of the photoactive layer to achieve the optimal overall absorption improvement. To get more support for these results, we compared the performance of the devices using poly(3-hexylthiophene) (P3HT) and [6,6]-phenyl-C_{61} butyric acid methyl ester ($PC_{61}BM$) (P3HT:$PC_{61}BM$) as the photovoltaic layer [Figure S11 (Supporting Information) and Table 1]. Compared to the devices without GO−Ag NPs, the devices with GO−Ag NPs exhibited an improved PCE, increased J_{sc}, and enhanced EQE due to the SPR effect of the GO−Ag NPs. These results are in accordance with those from the PBDTTT-C-T:$PC_{71}BM$ system, which further confirmed the SPR effect of GO−Ag NPs on device performance improvement.

To further discover the origin of the performance enhancement of the device with the SPR effect of GO−Ag NPs, the maximum photoinduced carriers generation rate (G_{max}) was quantitatively analyzed for the devices with and without GO−Ag NPs. Figure 4e presents the photocurrent density (J_{ph}) versus the effective applied voltage (V_{eff}) of the PSCs based on PEDOT:PSS and GO−Ag NPs/PEDOT:PSS under illumination at AM 1.5G (100 mW/cm^2). Here, the J_{ph} can be calculated using $J_{ph} = J_L - J_D$, where the J_D and J_L are the current density measured in the dark and under illumination, respectively.[53,54] V_{eff} is given by $V_{eff} = V_0 - V_a$, where V_0 and V_a are the voltage when J_{ph} is 0 and the applied bias voltage, respectively.[54,55] As shown in Figure 4e, the J_{ph} linearly increases at low V_{eff} and becomes fully saturated (saturation photocurrent density, J_{sat}) at high V_{eff} (above 2 V). When the V_{eff} is sufficiently high, attributed to the large electric potential, all the photogenerated excitons can dissociated and be collected by the corresponding electrodes to generate current. Therefore, J_{sat} can be determined as $J_{sat} = qG_{max}L$, where q and L are the electronic charge and the thickness of the photoactive layer, respectively.[54,56,57] Thus, the G_{max} can be calculated from the J_{sat}. The G_{max} for the devices without and with GO−Ag NPs are 9.68×10^{27} m^{-3} s^{-1} (J_{sat} = 15.5 mA/cm^2) and 1.12×10^{28} m^{-3} s^{-1} (J_{sat} = 17.9 mA/cm^2), respectively. Because the J_{sat} and G_{max} are only relative to the amount of absorbed photons of the devices, G_{max} can be regarded as a key factor for estimating the absorption capability of the devices. The noticeably improved G_{max} indicated the enhanced light-trapping ability of the device with the incorporation of the GO−Ag NPs, which well-agreed with the improvements in EQE, J_{sc}, and PCE.

Furthermore, the SPR effect of the GO−Ag NPs on the electrical characteristics of the device was examined through investigation of the exciton dissociation behavior of the devices without and with GO−Ag NPs. Figure 4f presents the exciton dissociation probabilities [$P(E,T)$] versus V_{eff} of the PSCs based on PEDOT:PSS and GO−Ag NPs/PEDOT:PSS under illumination at AM 1.5G (100 mW/cm^2). The J_{ph} of the devices can be given by $J_{ph} = qP(E,T)G_{max}L$.[55,57] Therefore, $P(E,T)$ can be determined by normalizing the photocurrent density with the saturation photocurrent density (J_{ph}/J_{sat}). As displayed in Figure 4f, the $P(E,T)$ of the device with GO−Ag NPs was higher than that without under short-circuit condition. The $P(E,T)$ was improved from 78.5% to 85.3% with the incorporation of GO−Ag NPs. This result demonstrated that the SPR effect of GO−Ag NPs could promote exciton dissociation, enhancing the charge collection and the photocurrent.

In addition, the steady-state PL measurements (inset of Figure 5) of the PBDTTT-C-T:$PC_{71}BM$ films on PEDOT:PSS and GO−Ag NPs/PEDOT:PSS were also performed to help understand the SPR effect of GO−Ag NPs on exciton generation. The PL spectrum of the sample with GO−Ag NPs shows a significantly enhanced PL intensity compared to the sample without GO−Ag NPs. Generally, the intensity of the steady-state PL is determined by two main factors: the plasmonic resonance frequency coupling between the photon absorption of polymer and the plasmonic field and the recombination rate of photogenerated excitons.[58,59] Herein, we attribute the PL enhancement to the overlap of the

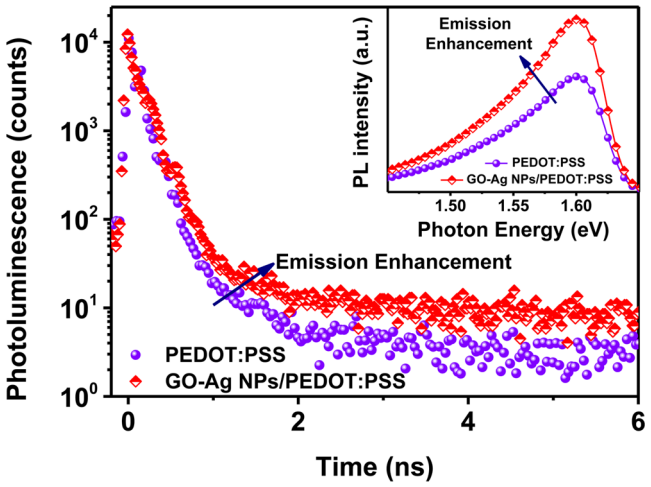

Figure 5. Photoluminescence decay profile of PBDTTT-C-T:$PC_{71}BM$ films on PEDOT:PSS and GO–Ag NPs/PEDOT:PSS. The inset presents the corresponding steady-state photoluminescence spectra of PBDTTT-C-T:$PC_{71}BM$ films on PEDOT:PSS and GO–Ag NPs/PEDOT:PSS.

plasmonic field with the photon absorption of the PBDTTT-C-T. To scrutinize the origin(s) of the change in exciton recombination rate and PL enhancement, TRPL spectroscopy was carried out (Figure 5). In the samples without GO–Ag NPs, a shorter exciton lifetime (216 ± 16 ps) was observed than the lifetime (327 ± 18 ps) of the samples with GO–Ag NPs. Commonly, a faster decay of excitons is correlated to higher exciton quenching and recombination losses.[19] The dramatically increased exciton lifetime after the incorporation of GO–Ag NPs is ascribed to the doughty coupling between excitons and the plasmonic field.[19,60] Hence, the enhancement in PL can be interpreted by the SPR effect of the GO–Ag NPs. The SPR effect of the GO–Ag NPs induced an improved absorption of PBDTTT-C-T by strong coupling with the plasmonic field, generating increased excitation rate and photogenerated excitons density and therefore higher PL intensity upon exciton recombination.[61,62]

CONCLUSIONS

In summary, a solution processable GO–Ag NPs was successfully prepared in situ and employed in PSCs at the interface of ITO/PEDOT:PSS with an enhanced SPR effect. The strong coupling between the SPR effect of GO–Ag NPs and incident light offers the possibility of improved light absorption capacity and corresponding exciton generation rate with enhanced charge collection, resulting in significant promotion in J_{sc} and thus PCE. The incorporation of GO–Ag NPs into PBDTTT-C-T:$PC_{71}BM$-based PSCs dramtically improved the PCE to 7.54% from 6.58%. These results demonstrated that the SPR GO–Ag NPs exhibited great potential as an effective alternative approach for high-efficiency PSCs. In addition, the synthetically simple, aqueous-solution-processable, cost-effective, and environmentally friendly GO–Ag NPs make it compatible with the roll-to-roll commercial manufacturing of printable PSCs.

EXPERIMENTAL SECTION

Synthesis of Graphene Oxide (GO). GO was synthesized through a modified Hummer's method.[63] Typically, 1.5 g of graphite, 1.5 g of $NaNO_3$, and 80 mL of concentrated H_2SO_4 were stirred in a flask for 15 min in an ice bath. Then, 12 g of the oxidizing agent $KMnO_4$ was added slowly and the mixture stirred for 2 h at 35 °C. Deionized water (120 mL) was added very slowly and the temperature increased to ~90 ± 5 °C. Finally, 15 mL of H_2O_2 (30%) in 200 mL of deionized water was added to end the reaction, and the color of the solution turned from brown to yellow. The obtained suspension was centrifuged and repeatedly washed with water to remove residue. The final product was dialyzed and dried under vacuum.

Synthesis of GO–Ag NPs and rGO–Ag NPs. Typically, GO was first dispersed in deionized water with sonication, and then $AgNO_3$ (99%, Sigma-Aldrich) was added followed with sonication to obtain a solution. The concentrations of both the GO and $AgNO_3$ were 0.5 mg/mL. Then, the solution was placed in a quartz reaction cell that was sealed with a cap and was deaerated by purging with N_2. The photochemical reduction process was performed by positioning the quartz cell about 5 cm from a UV lamp. After 25 min of irradiation, the mixture changed to dark brown. The final brown, aqueous solution of GO–Ag NPs nanocomposites was collected for solar cell fabrication. The rGO–Ag NPs was prepared using the same method as the synthesis of GO–Ag NPs.

Device Fabrication. The ITO-coated glass substrates were patterned by etching and ultrasonicated with detergent in deionized water, deionized water, acetone, and isopropyl alcohol for 15 min each following treatment with oxygen plasma for 10 min. The device architecture was ITO/GO–Ag NPs/PEDOT:PSS/active layer/LiF/Al. The GO–Ag NPs aqueous solution was spin-coated at 3000 rpm on cleaned ITO glass substrates for 1 min, and annealed at 80 °C for 5 min under N_2. The GO–Ag NPs layer was covered by spin-coating PEDOT:PSS (Baytron P VP A1 4083) at 4000 rpm for 1 min. After annealing at 150 °C for 15 min, the photoactive layer of PBDTTT-C-T:$PC_{71}BM$ solution [1:1.5 w/w in 1,2-dichlorobenzene (DCB) with 1,8-diiodooctane, 3%, v/v] was spin-coated at 1000 rpm for 2 min in a glovebox filled with N_2. For the devices incorporated with P3HT:$PC_{61}BM$ photoactive layers, a mixture of P3HT and $PC_{61}BM$ (1:1, w/w) in DCB was spin-coated at 800 rpm on the top of the PEDOT:PSS layer for 30 s. After the photoactive layer was dried, a 1 nm interfacial layer of LiF was deposited, and a 100 nm thick Al electrode was thermally deposited to complete the device with an active area of 0.04 cm^2 controlled by a shadow mask.

Characterization. The nanomorphologies of GO and GO–Ag NPs were characterized by atomic force microscopy (AFM, Digital Instrumental Nanoscope 31), laser scanning confocal microscopy (LSCM, CarlZeiss LSM710), transmission electron microscopy (TEM), and high-resolution transmission electron microscopy (HRTEM) (JEOL, JEM-2100F). The TEM and HRTEM samples were prepared by transferring GO–Ag NPs onto a copper grid. The absorption spectra of GO and GO–Ag NPs and the reflectance spectra of the active layers were collected with a Lambda 750 (PerkinElmer) UV–vis–NIR spectrophotometer. The steady-state photoluminescence spectra were measured with a Hitachi F-7000 spectrometer, and the time-resolved photoluminescence (TRPL) measurements was carried out with a Edinburgh Instrument FLS920. Raman spectroscopy profiles were collected with a LabRam-1B Raman microscope. The X-ray photoelectron spectroscopy (XPS) spectra were performed with a Kratos AXIS Ultra XPS system, and an AXIS-ULTRA DLD spectrometer (Kratos Analytical Ltd.) was employed to collect the ultraviolet photoelectron spectroscopy (UPS) spectra. The surface nanomorphologies of the PEDOT:PSS and GO–Ag NPs/PEDOT:PSS layers before and after being covered with photoactive layers were investigated by AFM in tapping mode. The current–voltage (J–V) curves were investigated under simulated AM 1.5 G (100 mW/cm^2, Abet Solar Simulator Sun2000) irradiation and in the dark and recorded with a Keithley 2400 Source Meter. The external quantum efficiency (EQE) measurements were performed under monochromatic illumination.

■ ASSOCIATED CONTENT

Supporting Information

Flowchart of the synthesis of GO−Ag as a function of UV irradiation time; TEM and AFM images of GO and GO−Ag; AFM images of PEDOT:PSS and GO−Ag NPs/PEDOT:PSS films on ITO glass substrate before and after being covered with PBDTTT-C-T:$PC_{71}BM$ films; TEM images of GO−Ag NPs prepared with different UV irradiation times; UPS of PEDOT:PSS and GO−Ag NPs/PEDOT:PSS films; reflectance of the devices based on PBDTTT-C-T:$PC_{71}BM$ without and with GO−Ag NPs; XPS C 1s spectra of GO after thermal annealing at 150 °C for 15 min; *J*−*V* characteristics of GO/PEDOT:PSS-, Ag NPs/PEDOT:PSS-, and rGO−Ag NPs/PEDOT:PSS-based devices and devices without and with GO−Ag NPs prepared with different UV irradiation times; and *J*−*V* curves and EQE and ΔEQE spectra of devices based on P3HT:$PC_{61}BM$. This material is available free of charge via the Internet at http://pubs.acs.org.

■ AUTHOR INFORMATION

Corresponding Author

*Tel: +86 791 83969562. Fax: +86 791 83969561. E-mail: ywchen@ncu.edu.cn.

Notes

The authors declare no competing financial interest.

■ ACKNOWLEDGMENTS

This work was supported by the National Natural Science Foundation of China (51273088, 51263016 and 51473075), National Basic Research Program of China (973 Program 2014CB260409), National Science Fund for Distinguished Young Scholars (51425304), and Doctoral Programs Foundation of Ministry of Education of China (Grants 20133601110004).

■ REFERENCES

(1) Li, G.; Zhu, R.; Yang, Y. Polymer Solar Cells. *Nat. Photonics* **2012**, *6*, 153−161.

(2) Günes, S.; Neugebauer, H.; Sariciftci, N. S. Conjugated Polymer-Based Organic Solar Cells. *Chem. Rev.* **2007**, *107*, 1324−1338.

(3) Heeger, A. J. 25th Anniversary Article: Bulk Heterojunction Solar Cells: Understanding the Mechanism of Operation. *Adv. Mater.* **2014**, *26*, 10−28.

(4) Dou, L.; You, J.; Hong, Z.; Xu, Z.; Li, G.; Street, R. A.; Yang, Y. 25th Anniversary Article: A Decade of Organic/Polymeric Photovoltaic Research. *Adv. Mater.* **2013**, *25*, 6642−6671.

(5) Krebs, F. C.; Espinosa, N.; Hösel, M.; Søndergaard, R. R.; Jørgensen, M. 25th Anniversary Article: Rise to Power—OPV-Based Solar Parks. *Adv. Mater.* **2014**, *26*, 29−39.

(6) He, Z.; Zhong, C.; Su, S.; Xu, M.; Wu, H.; Cao, Y. Enhanced Power-Conversion Efficiency in Polymer Solar Cells Using an Inverted Device Structure. *Nat. Photonics* **2012**, *6*, 593−597.

(7) You, J.; Dou, L.; Yoshimura, K.; Kato, T.; Ohya, K.; Moriarty, T.; Emery, K.; Chen, C. C.; Gao, J.; Li, G.; et al. A Polymer Tandem Solar Cell with 10.6% Power Conversion Efficiency. *Nat. Commun.* **2013**, *4*, 1446.

(8) Chen, C. C.; Chang, W. H.; Yoshimura, K.; Ohya, K.; You, J.; Gao, J.; Hong, Z.; Yang, Y. An Efficient Triple-Junction Polymer Solar Cell Having a Power Conversion Efficiency Exceeding 11%. *Adv. Mater.* **2014**, *26*, 5670−5677.

(9) Li, Y. Molecular Design of Photovoltaic Materials for Polymer Solar Cells: Toward Suitable Electronic Energy Levels and Broad Absorption. *Acc. Chem. Res.* **2012**, *45*, 723−733.

(10) Henson, Z. B.; Mullen, K.; Bazan, G. C. Design Strategies for Organic Semiconductors Beyond the Molecular Formula. *Nat. Chem.* **2012**, *4*, 699−704.

(11) Ye, L.; Zhang, S.; Huo, L.; Zhang, M.; Hou, J. Molecular Design toward Highly Efficient Photovoltaic Polymers Based on Two-Dimensional Conjugated Benzodithiophene. *Acc. Chem. Res.* **2014**, *47*, 1595−1603.

(12) Dang, M. T.; Hirsch, L.; Wantz, G.; Wuest, J. D. Controlling the Morphology and Performance of Bulk Heterojunctions in Solar Cells. Lessons Learned from the Benchmark Poly(3-hexylthiophene):[6,6]-Phenyl-C_{61}-butyric Acid Methyl Ester System. *Chem. Rev.* **2013**, *113*, 3734−3765.

(13) Yang, L.; Zhou, H.; Price, S. C.; You, W. Parallel-like Bulk Heterojunction Polymer Solar Cells. *J. Am. Chem. Soc.* **2012**, *134*, 5432−5435.

(14) Kim, J. B.; Kim, P.; Pegard, N. C.; Oh, S. J.; Kagan, C. R.; Fleischer, J. W.; Stone, H. A.; Loo, Y.-L. Wrinkles and Deep Folds as Photonic Structures in Photovoltaics. *Nat. Photonics* **2012**, *6*, 327−332.

(15) Huang, F.; Wu, H.; Cao, Y. Water/Alcohol Soluble Conjugated Polymers as Highly Efficient Electron Transporting/Injection Layer in Optoelectronic Devices. *Chem. Soc. Rev.* **2010**, *39*, 2500.

(16) Yip, H.-L.; Jen, A. K. Y. Recent Advances in Solution-Processed Interfacial Materials for Efficient and Stable Polymer Solar Cells. *Energy Environ. Sci.* **2012**, *5*, 5994.

(17) Liu, S.; Zhang, K.; Lu, J.; Zhang, J.; Yip, H.-L.; Huang, F.; Cao, Y. High-Efficiency Polymer Solar Cells Via the Incorporation of an Amino-Functionalized Conjugated Metallopolymer as a Cathode Interlayer. *J. Am. Chem. Soc.* **2013**, *135*, 15326−15329.

(18) Kumar, A.; Rosen, N.; Devine, R.; Yang, Y. Interface Design To Improve Stability of Polymer Solar Cells for Potential Space Applications. *Energy Environ. Sci.* **2011**, *4*, 4917.

(19) Wu, J.-L.; Chen, F.-C.; Hsiao, Y.-S.; Chien, F.-C.; Chen, P.; Kuo, C.-H.; Huang, M. H.; Hsu, C.-S. Surface Plasmonic Effects of Metallic Nanoparticles on the Performance of Polymer Bulk Heterojunction Solar Cells. *ACS Nano* **2011**, *5*, 959−967.

(20) Jo, J.; Na, S.-I.; Kim, S.-S.; Lee, T.-W.; Chung, Y.; Kang, S.-J.; Vak, D.; Kim, D.-Y. Three-Dimensional Bulk Heterojunction Morphology for Achieving High Internal Quantum Efficiency in Polymer Solar Cells. *Adv. Funct. Mater.* **2009**, *19*, 2398−2406.

(21) Park, S. H.; Roy, A.; Beaupre, S.; Cho, S.; Coates, N.; Moon, J. S.; Moses, D.; Leclerc, M.; Lee, K.; Heeger, A. J. Bulk Heterojunction Solar Cells with Internal Quantum Efficiency Approaching 100%. *Nat. Photonics* **2009**, *3*, 297−302.

(22) Gan, Q.; Bartoli, F. J.; Kafafi, Z. H. Plasmonic-Enhanced Organic Photovoltaics: Breaking the 10% Efficiency Barrier. *Adv. Mater.* **2013**, *25*, 2385−2396.

(23) Wang, D. H.; Kim, D. Y.; Choi, K. W.; Seo, J. H.; Im, S. H.; Park, J. H.; Park, O. O.; Heeger, A. J. Enhancement of Donor−Acceptor Polymer Bulk Heterojunction Solar Cell Power Conversion Efficiencies by Addition of Au Nanoparticles. *Angew. Chem., Int. Ed.* **2011**, *50*, 5519−5523.

(24) Choi, H.; Lee, J.-P.; Ko, S.-J.; Jung, J.-W.; Park, H.; Yoo, S.; Park, O.; Jeong, J.-R.; Park, S.; Kim, J. Y. Multipositional Silica-Coated Silver Nanoparticles for High-Performance Polymer Solar Cells. *Nano Lett.* **2013**, *13*, 2204−2208.

(25) Choi, H.; Ko, S.-J.; Choi, Y.; Joo, P.; Kim, T.; Lee, B. R.; Jung, J.-W.; Choi, H. J.; Cha, M.; Jeong, J.-R.; et al. Versatile Surface Plasmon Resonance of Carbon-Dot-Supported Silver Nanoparticles in Polymer Optoelectronic Devices. *Nat. Photonics* **2013**, *7*, 732−738.

(26) Liu, J.; Durstock, M.; Dai, L. Graphene Oxide Derivatives as Hole- and Electron-Extraction Layers for High-Performance Polymer Solar Cells. *Energy Environ. Sci.* **2014**, *7*, 1297.

(27) Wang, D. H.; Kim, J. K.; Seo, J. H.; Park, I.; Hong, B. H.; Park, J. H.; Heeger, A. J. Transferable Graphene Oxide by Stamping Nanotechnology: Electron-Transport Layer for Efficient Bulk−Heterojunction Solar Cells. *Angew. Chem., Int. Ed.* **2013**, *52*, 2874−2880.

(28) Liu, J.; Xue, Y.; Gao, Y.; Yu, D.; Durstock, M.; Dai, L. Hole and Electron Extraction Layers Based on Graphene Oxide Derivatives for

High-Performance Bulk Heterojunction Solar Cells. *Adv. Mater.* **2012**, *24*, 2228−2233.
(29) Bonaccorso, F.; Sun, Z.; Hasan, T.; Ferrari, A. C. Graphene Photonics and Optoelectronics. *Nat. Photonics* **2010**, *4*, 611−622.
(30) Yuan, K.; Chen, L.; Tan, L.; Chen, Y. Performance Enhancement of Bulk Heterojunction Solar Cells with Direct Growth of CdS-Cluster-Decorated Graphene Nanosheets. *Chem.—Eur. J.* **2014**, *20*, 6010−6018.
(31) Li, S.-S.; Tu, K.-H.; Lin, C.-C.; Chen, C.-W.; Chhowalla, M. Solution-Processable Graphene Oxide as an Efficient Hole Transport Layer in Polymer Solar Cells. *ACS Nano* **2010**, *4*, 3169−3174.
(32) Yun, J.-M.; Yeo, J.-S.; Kim, J.; Jeong, H.-G.; Kim, D.-Y.; Noh, Y.-J.; Kim, S.-S.; Ku, B.-C.; Na, S.-I. Solution-Processable Reduced Graphene Oxide as a Novel Alternative to PEDOT:PSS Hole Transport Layers for Highly Efficient and Stable Polymer Solar Cells. *Adv. Mater.* **2011**, *23*, 4923−4928.
(33) Dutta, S.; Ray, C.; Sarkar, S.; Pradhan, M.; Negishi, Y.; Pal, T. Silver Nanoparticle Decorated Reduced Graphene Oxide (rGO) Nanosheet: A Platform for SERS Based Low-Level Detection of Uranyl Ion. *ACS Appl. Mater. Interfaces* **2013**, *5*, 8724−8732.
(34) Xu, W.-P.; Zhang, L.-C.; Li, J.-P.; Lu, Y.; Li, H.-H.; Ma, Y.-N.; Wang, W.-D.; Yu, S.-H. Facile Synthesis of Silver@Graphene Oxide Nanocomposites and Their Enhanced Antibacterial Properties. *J. Mater. Chem.* **2011**, *21*, 4593−4597.
(35) Salam, N.; Sinha, A.; Roy, A. S.; Mondal, P.; Jana, N. R.; Islam, S. M. Synthesis of Silver−Graphene Nanocomposite and Its Catalytic Application for the One-Pot Three-Component Coupling Reaction and One-Pot Synthesis of 1,4-Disubstituted 1,2,3-Triazoles in Water. *RSC Adv.* **2014**, *4*, 10001−10012.
(36) Tran, Q. T.; Hoa, H. T. M.; Yoo, D.-H.; Cuong, T. V.; Hur, S. H.; Chung, J. S.; Kim, E. J.; Kohl, P. A. Reduced Graphene Oxide as an Over-Coating Layer on Silver Nanostructures for Detecting NH_3 Gas at Room Temperature. *Sens. Actuators B* **2014**, *194*, 45−50.
(37) Fan, G.-Q.; Zhuo, Q.-Q.; Zhu, J.-J.; Xu, Z.-Q.; Cheng, P.-P.; Li, Y.-Q.; Sun, X.-H.; Lee, S.-T.; Tang, J.-X. Plasmonic-Enhanced Polymer Solar Cells Incorporating Solution-Processable Au Nanoparticle−Adhered Graphene Oxide. *J. Mater. Chem.* **2012**, *22*, 15614−15619.
(38) Huo, L.; Zhang, S.; Guo, X.; Xu, F.; Li, Y.; Hou, J. Replacing Alkoxy Groups with Alkylthienyl Groups: A Feasible Approach To Improve the Properties of Photovoltaic Polymers. *Angew. Chem., Int. Ed.* **2011**, *50*, 9697−9702.
(39) Wu, T.; Liu, S.; Luo, Y.; Lu, W.; Wang, L.; Sun, X. Surface Plasmon Resonance-Induced Visible Light Photocatalytic Reduction of Graphene Oxide: Using Ag Nanoparticles as a Plasmonic Photocatalyst. *Nanoscale* **2011**, *3*, 2142−2144.
(40) Tang, X.-Z.; Cao, Z.; Zhang, H.-B.; Liu, J.; Yu, Z.-Z. Growth of Silver Nanocrystals on Graphene by Simultaneous Reduction of Graphene Oxide and Silver Ions with a Rapid and Efficient One-Step Approach. *Chem. Commun.* **2011**, *47*, 3084−3086.
(41) Guardia, L.; Villar-Rodil, S.; Paredes, J. I.; Rozada, R.; Martínez-Alonso, A.; Tascón, J. M. D. UV Light Exposure of Aqueous Graphene Oxide Suspensions To Promote Their Direct Reduction, Formation of Graphene−Metal Nanoparticle Hybrids and Dye Degradation. *Carbon* **2012**, *50*, 1014−1024.
(42) Tang, X.-Z.; Li, X.; Cao, Z.; Yang, J.; Wang, H.; Pu, X.; Yu, Z.-Z. Synthesis of Graphene Decorated with Silver Nanoparticles by Simultaneous Reduction of Graphene Oxide and Silver Ions with Glucose. *Carbon* **2013**, *59*, 93−99.
(43) Zhang, Z.; Xu, F.; Yang, W.; Guo, M.; Wang, X.; Zhang, B.; Tang, J. A Facile One-Pot Method to High-Quality Ag−Graphene Composite Nanosheets for Efficient Surface-Enhanced Raman Scattering. *Chem. Commun.* **2011**, *47*, 6440−6442.
(44) Li, S.-K.; Yan, Y.-X.; Wang, J.-L.; Yu, S.-H. Bio-Inspired in Situ Growth of Monolayer Silver Nanoparticles on Graphene Oxide Paper as Multifunctional Substrate. *Nanoscale* **2013**, *5*, 12616−12623.
(45) Dutta, S.; Sarkar, S.; Ray, C.; Roy, A.; Sahoo, R.; Pal, T. Mesoporous Gold and Palladium Nanoleaves from Liquid−Liquid Interface: Enhanced Catalytic Activity of the Palladium Analogue toward Hydrazine-Assisted Room-Temperature 4-Nitrophenol Reduction. *ACS Appl. Mater. Interfaces* **2014**, *6*, 9134−9143.
(46) Linic, S.; Christopher, P.; Ingram, D. B. Plasmonic-Metal Nanostructures for Efficient Conversion of Solar to Chemical Energy. *Nat. Mater.* **2011**, *10*, 911−921.
(47) Wang, X.; Meng, G.; Zhu, C.; Huang, Z.; Qian, Y.; Sun, K.; Zhu, X. A Generic Synthetic Approach to Large-Scale Pristine-Graphene/Metal-Nanoparticles Hybrids. *Adv. Funct. Mater.* **2013**, *23*, 5771−5777.
(48) Yin, H.; Tang, H.; Wang, D.; Gao, Y.; Tang, Z. Facile Synthesis of Surfactant-Free Au Cluster/Graphene Hybrids for High-Performance Oxygen Reduction Reaction. *ACS Nano* **2012**, *6*, 8288−8297.
(49) Li, Q.; Guo, B.; Yu, J.; Ran, J.; Zhang, B.; Yan, H.; Gong, J. R. Highly Efficient Visible-Light-Driven Photocatalytic Hydrogen Production of CdS-Cluster-Decorated Graphene Nanosheets. *J. Am. Chem. Soc.* **2011**, *133*, 10878−10884.
(50) Williams, G.; Seger, B.; Kamat, P. V. TiO_2−Graphene Nanocomposites. UV-Assisted Photocatalytic Reduction of Graphene Oxide. *ACS Nano* **2008**, *2*, 1487−1491.
(51) Ding, Y. H.; Zhang, P.; Zhuo, Q.; Ren, H. M.; Yang, Z. M.; Jiang, Y. A Green Approach to the Synthesis of Reduced Graphene Oxide Nanosheets under UV Irradiation. *Nanotechnology* **2011**, *22*, 215601.
(52) Sergeant, N. P.; Hadipour, A.; Niesen, B.; Cheyns, D.; Heremans, P.; Peumans, P.; Rand, B. P. Design of Transparent Anodes for Resonant Cavity Enhanced Light Harvesting in Organic Solar Cells. *Adv. Mater.* **2012**, *24*, 728−732.
(53) Cowan, S. R.; Roy, A.; Heeger, A. J. Recombination in Polymer−Fullerene Bulk Heterojunction Solar Cells. *Phys. Rev. B* **2010**, *82*, 245207.
(54) Kyaw, A. K. K.; Wang, D. H.; Wynands, D.; Zhang, J.; Nguyen, T.-Q.; Bazan, G. C.; Heeger, A. J. Improved Light Harvesting and Improved Efficiency by Insertion of an Optical Spacer (ZnO) in Solution-Processed Small-Molecule Solar Cells. *Nano Lett.* **2013**, *13*, 3796−3801.
(55) Tan, K.-S.; Chuang, M.-K.; Chen, F.-C.; Hsu, C.-S. Solution-Processed Nanocomposites Containing Molybdenum Oxide and Gold Nanoparticles as Anode Buffer Layers in Plasmonic-Enhanced Organic Photovoltaic Devices. *ACS Appl. Mater. Interfaces* **2013**, *5*, 12419−12424.
(56) Mihailetchi, V. D.; Koster, L. J. A.; Hummelen, J. C.; Blom, P. W. M. Photocurrent Generation in Polymer−Fullerene Bulk Heterojunctions. *Phys. Rev. Lett.* **2004**, *93*, 216601.
(57) Mihailetchi, V. D.; Xie, H. X.; de Boer, B.; Koster, L. J. A.; Blom, P. W. M. Charge Transport and Photocurrent Generation in Poly(3-hexylthiophene):Methanofullerene Bulk-Heterojunction Solar Cells. *Adv. Funct. Mater.* **2006**, *16*, 699−708.
(58) Jung, K.; Song, H.-J.; Lee, G.; Ko, Y.; Ahn, K.; Choi, H.; Kim, J. Y.; Ha, K.; Song, J.; Lee, J.-K.; et al. Plasmonic Organic Solar Cells Employing Nanobump Assembly Via Aerosol-Derived Nanoparticles. *ACS Nano* **2014**, *8*, 2590−2601.
(59) Wang, J.; Lee, Y.-J.; Chadha, A. S.; Yi, J.; Jespersen, M. L.; Kelley, J. J.; Nguyen, H. M.; Nimmo, M.; Malko, A. V.; Vaia, R. A.; et al. Effect of Plasmonic Au Nanoparticles on Inverted Organic Solar Cell Performance. *J. Phys. Chem. C* **2012**, *117*, 85−91.
(60) Zhu, X. Y.; Yang, Q.; Muntwiler, M. Charge-Transfer Excitons at Organic Semiconductor Surfaces and Interfaces. *Acc. Chem. Res.* **2009**, *42*, 1779−1787.
(61) Wu, B.; Oo, T. Z.; Li, X.; Liu, X.; Wu, X.; Yeow, E. K. L.; Fan, H. J.; Mathews, N.; Sum, T. C. Efficiency Enhancement in Bulk-Heterojunction Solar Cells Integrated with Large-Area Ag Nanotriangle Arrays. *J. Phys. Chem. C* **2012**, *116*, 14820−14825.
(62) Mahmoud, M. A.; Poncheri, A. J.; Phillips, R. L.; El-Sayed, M. A. Plasmonic Field Enhancement of the Exciton−Exciton Annihilation Process in a Poly(*p*-phenyleneethynylene) Fluorescent Polymer by Ag Nanocubes. *J. Am. Chem. Soc.* **2010**, *132*, 2633−2641.
(63) Jahan, M.; Bao, Q.; Yang, J.-X.; Loh, K. P. Structure-Directing Role of Graphene in the Synthesis of Metal−Organic Framework Nanowire. *J. Am. Chem. Soc.* **2010**, *132*, 14487−14495.